**Journal of Nuclear Medicine, published on October 7, 2021 as doi:10.2967/jnumed.121.262427**



# First-in-human brain PET imaging of the GluN2B-containing N-methyl-D-aspartate receptor with *(R)*-$^{11}$C-Me-NB1

Lucas Rischka[1,*], Chrysoula Vraka[2,*], Verena Pichler[2,3], Sazan Rasul[2], Lukas Nics[2], Gregor Gryglewski[1], Patricia Handschuh[1], Matej Murgaš[1], Godber M. Godbersen[1], Leo R. Silberbauer[1], Jakob Unterholzner[1], Christoph Wotawa[1], Ahmed Haider[4], Hazem Ahmed[4], Roger Schibli[4], Thomas Mindt[2,5,6], Markus Mitterhauser[2,5], Wolfgang Wadsak[2,7], Andreas Hahn[1], Rupert Lanzenberger[1,#],Marcus Hacker[2,#], Simon M. Ametamey[4,#]

(*contributed equally, [#]corresponding authors)

[1]*Department of Psychiatry and Psychotherapy, Medical University of Vienna, Vienna, Austria*

[2]*Department of Biomedical Imaging and Image-guided Therapy, Division of Nuclear Medicine, Medical University of Vienna, Vienna, Austria*

[3]*Department of Pharmaceutical Chemistry, University of Vienna, Vienna, Austria*

[4]*Centre for Radiopharmaceutical Sciences ETH-PSI-USZ, Institute of Pharmaceutical Sciences ETH, Zurich, Switzerland*

[5]*Ludwig Boltzmann Institute Applied Diagnostics, Vienna, Austria*

[6]*Institute of Inorganic Chemistry, Faculty of Chemistry, University of Vienna, Vienna, Austria*

[7]*Center for Biomarker Research in Medicine (CBmed), Graz, Austria*

Running title: GluN2B subunit imaging in humans

For submission to

**Journal of Nuclear Medicine**

| Word count | 303 | Abstract |
|---|---|---|
| | 3107 | Article Body |
| Figures: 5, References: 27<br>Supplementary Material: 5 Figures, 2 Tables | | |

**Corresponding authors:**

Prof. Dr. Simon M. Ametamey
Radiopharmaceutical Sciences, ETH Zurich
Institute of Pharmaceutical Sciences
Vladimir-Prelog-Weg 1-5/10, CH-8093 Zurich, Switzerland
Telephone: +41 44 6337463
Fax: +41 44 6331367
E-mail: simon.ametamey@pharma.ethz.ch

Prof. Dr. Marcus Hacker
Department of Biomedical Imaging and Image-guided Therapy
Division of Nuclear Medicine, Medical University of Vienna, Austria
Waehringer Guertel 18-20, 1090 Vienna, Austria
Telephone: +43 1 40400-55300
E-mail: marcus.hacker@meduniwien.ac.at

Prof. Dr. Rupert Lanzenberger
Department of Psychiatry and Psychotherapy, Medical University of Vienna, Austria
Waehringer Guertel 18-20, 1090 Vienna, Austria
Telephone: +43 1 40400-35760
E-mail: rupert.lanzenberger@meduniwien.ac.at

**First authors:**

Lucas Rischka, MSc
Department of Psychiatry and Psychotherapy, Medical University of Vienna, Austria
Waehringer Guertel 18-20, 1090 Vienna, Austria
Telephone: +43 1 40400-23220
E-mail: lucas.rischka@meduniwien.ac.at
Profession: research fellow and PhD-student

Dr. Chysoula Vraka
Department of Biomedical Imaging and Image-guided Therapy
Division of Nuclear Medicine, Medical University of Vienna, Austria
Waehringer Guertel 18-20, 1090 Vienna, Austria
Telephone: 01 40400-55450
E-mail: chrysoula.vraka@meduniwien.ac.at

**Financial support:** This project was supported in part by the Swiss National Science Foundation grant numbers 310030E-160403/1 and 310030E-182872/1 to Prof. Simon M. Ametamey. Matej Murgaš is funded by the Austrian Science Fund FWF DOC 33-B27. Leo R. Silberbauer is a recipient of a DOC fellowship of the Austrian Academy of Sciences.

## ABSTRACT

The N-methyl-D-aspartate receptor (NMDAR) plays a crucial role in neurodegenerative diseases such as Alzheimer's disease and in the treatment of major depression by new fast-acting antidepressants such as ketamine. Given their broad implications, GluN2B-containing NMDARs have been of large interest as diagnostic and therapeutic targets. Recently, *(R)*-$^{11}$C-Me-NB1 was investigated preclinically and shown to be a promising radioligand for imaging GluN2B subunits. Here, we report on the performance characteristics of this novel radioligand in a first-in-human PET study. **Methods**: Six healthy male subjects were scanned twice on a fully-integrated PET/MR scanner with *(R)*-$^{11}$C-Me-NB1 for 120 min. Brain uptake and tracer distribution over time were investigated by standardized uptake values (SUV). Test-retest reliability was assessed with the absolute percentage difference (APD) and the coefficient of variation (COV). Exploratory total volumes of distribution ($V_T$) were computed using an arterial input function and the Logan plot as well as a constrained two-tissue compartment model with $K_1/k_2$ coupled (2TCM). SUV was correlated with $V_T$ to investigate its potential as a surrogate marker of GluN2B expression. **Results**: High and heterogeneous radioligand uptake was observed across the entire gray matter with reversible kinetics within the scan time. SUV APD ranged from 6.8 - 8.5% and COV from 4.9 - 6.0%, indicating a high test-retest reliability. A moderate correlation was found between SUV averaged from 70-90 min and $V_T$ using Logan plot (Spearman's rho = 0.44). Correlation between $V_T$ Logan and 2TCM was r= 0.76. **Conclusion**: The novel radioligand, *(R)*-$^{11}$C-Me-NB1, was highly effective in mapping GluN2B-enriched NMDARs in the human brain. With a heterogeneous uptake and a high test-retest reliability, this radioligand offers promise to deepen our understanding of the GluN2B-containing NMDA receptor in the pathophysiology and treatment of neuropsychiatric disease such as Alzheimer's disease and major depression. Additionally, it could help in the selection of appropriate doses of GluN2B-targeting drugs.

## Keywords:

Glutamate, N-methyl-D-aspartate (NMDA), GluN2B-subunits, neurodegenerative disease, positron emission tomography (PET)

# INTRODUCTION

The *N*-Methyl-D-aspartate receptor (NMDAR) constitutes a heterotetrameric glutamate-gated ion channel that mediates key physiological functions such as synaptic transmission, plasticity and higher cognitive functions in the mammalian central nervous system (*1*,*2*). Despite their homeostatic relevance, NMDARs trigger pathophysiological processes upon excessive activation, thereby prompting apoptotic cascades that ultimately result in neurodegeneration (*3*). Moreover, NMDAR dysfunctions have been implicated in a multitude of neuropsychiatric disorders including Alzheimer's disease, vascular dementia, Parkinson's disease, stroke, traumatic brain injury, depression and schizophrenia (*4*,*5*). Recent studies demonstrated that activation of extrasynaptic NMDARs, which are typically enriched with the GluN2B subunit, resulted in excitotoxicity, while activation of synaptic NMDARs had protective effects (*4*). As such, subtype-selective modulation of GluN2B-containing NMDARs has been suggested as a promising drug development strategy that would provide therapeutic efficacy, while concurrently sparing physiological NMDAR functions (*6*,*7*). Despite strenuous research and development efforts, GluN2B-selective antagonists showed only limited clinical efficacy so far (*8*). While underlying causes may have been of multifactorial origin, it has been suggested that the availability of an appropriate GluN2B-targeted probe would facilitate drug development (*9*). Indeed, a radioligand to visualize GluN2B-containing NMDARs in the living human brain is currently lacking. Thus, it is of paramount value to develop such tools to further elucidate the versatile roles of GluN2B-containing NMDARs in neurodegenerative and other neuropsychiatric diseases, as well as to guide future drug development efforts via target engagement studies.

Despite the plethora of attempts to develop a suitable NMDAR positron emission tomography (PET) radioligand, the majority of reported probes suffered from major drawbacks such as low brain uptake, radiometabolites entering the brain, prominent off-target binding particularly to σ1 receptors, and brain uptake inconsistent with the known expression profile (*10*,*11*). To date, the most promising structural class of GluN2B-targeted PET radioligands are

the *2,3,4,5*-tetrahydro-1H-benzazepine derivatives (*12–15*). A recent publication by Haider et al. reported on the benzazepine derivative, *(R)*-$^{11}$C-Me-NB1 (Figure 1), as a potential PET radioligand for imaging the GluN2B-containing NMDARs. Biodistribution and PET imaging studies in rodents showed an uptake pattern in brain regions known to express the GluN2B subunits of the NMDAR with the lowest uptake in the cerebellum, a brain region known to have low to negligible GluN2B-subunits in rodents. Specificity of *(R)*-$^{11}$C-Me-NB1 binding was substantiated in blocking studies in a dose-dependent manner and selectivity over σ1 receptors was confirmed using σ1 receptor knockout mice (*15*).

Considering the promising characteristics of this radioligand in rodents, the current work aims to translate the utility of *(R)*-$^{11}$C-Me-NB1 for imaging the GluN2B-subunits of the NMDAR to humans. To the best of our knowledge, this work signifies the first assessment of a GluN2B PET imaging probe in the living human brain.

# METHODS

## Participants and study design

Six healthy male subjects (mean age = 23.3 ± 2.9) were recruited for the study. All participants were free from internal, neurological or psychiatric disorders assessed via a thorough medical history, physical examination, electrocardiogram and routine laboratory parameters. Exclusion criteria were neurological diseases or psychiatric disorders, illness 2 weeks prior to recruitment, history of drug or atopic allergy, myocardial infarction, history of cancer, liver or renal disease, family history of prolonged QT-interval, magnetic resonance imaging (MRI) or PET contraindications, consumption of tobacco products 3 months before recruitment, history of drug or alcohol abuse and significant prior radiation exposure in the past 10 years. After detailed explanation of the study design, all subjects gave written informed consent. The study was registered in the EudraCT database (2018-002933-39) and approved by the Ethics Committee of the Medical University of Vienna (ethics number: 1980/2018). Procedures were carried out in accordance with the Declaration of Helsinki. Subjects were reimbursed for participation.

## Tracer preparation

*(R)*-$^{11}$C-Me-NB1 was produced on a fully-automated GE Tracerlab™ FX2 C synthesis module by applying $^{11}C\text{-}CO_2$ from a GE PETtrace™ 860. $^{11}C\text{-}CH_3I$ was reacted with the enantiomerically pure des-methyl GMP-grade precursor *(R)*-NB1 in DMF and in the presence of $Cs_2CO_3$ following previously published procedures (*15*). Minor synthetic adaptations included the use of a SupelcosilTM LC-ABZ+ column (5 µm, 250 mm × 10 mm; Bellonte, USA) and a mobile phase of 60% acetonitrile / 40% aqueous $Na_2HPO_4$ (0.02 mol/L) for the final product purification. After high performance liquid chromatography (HPLC) purification, the product was trapped on a Sep-Pak® Plus, C18 Cartridges (Waters, Milford, USA), washed with 10 mL $H_2O$ ad inj., eluted with 1.5 mL of ethanol, and formulated for human application using 10 mL of NaCl (0.9%) and 6

mL of phosphate-buffered saline. Product quality was assessed according to the guidance of radiopharmaceutical preparations of the European Pharmacopoeia (*16*). Molar activities were calculated through assessment of radioactivity at the end of synthesis and determination of non-radioactive *(R)*-Me-NB1 via HPLC. Values were decay corrected to the time of tracer administration.

## PET imaging

All participants underwent two measurements on a fully-integrated PET/MR scanner (Siemens mMR Biograph, Erlangen, Germany) lasting for 120 min. The mean interval between the scans was 18.2 ± 8.8 days (range 6 – 28 days) and measurements started between 4.30 and 6.00 p.m. CET (mean difference between the measurement start times = 21 ± 24 min, range 0 – 60 min). PET data were acquired in 3D list-mode. The radioligand, *(R)*-$^{11}$C-Me-NB1, was administered as a bolus through a cubital vein (mean injected dose: 448 ± 34 MBq; 5.98 ± 0.85 MBq/kg body weight; 0.15 ± 0.11 nmol/kg body weight, one value was excluded because of technical HPLC issues). There were no adverse events or clinically detectable pharmacological effects in any of the subjects. No changes in vital signs, laboratory results or electrocardiograms were observed. During the scan, subjects were instructed not to fall asleep, to observe a black crosshair on a grey background presented on a screen at the end of the gantry, to let their thoughts wander and not to move any body part. Additionally, head movement was minimized with stabilizing cushions within the head coil.

## Arterial blood sampling, metabolite analyses, and arterial input function

Before each measurement, arterial and venous cannulas were inserted in the radial artery and a cubital vein of the opposite arm for arterial blood sampling and administration of the radioligand. Arterial blood was drawn automatically for the first 6 minutes (Twilite II system, Swisstrace, Menzingen, Switzerland). Manual blood samples were taken at 3, 4, 5, 10, 20, 30,

40, 60, 80, 100 and 120 min and were immediately measured in a gamma counter (Wizard², 3”; Perkin Elmer), for whole blood activity and, after centrifugation, for plasma activity. The gamma counter was cross-calibrated to the PET/MR scanner. Radiometabolites were determined for the time points 5, 10, 20, 30, 40, and 60 min by HPLC using an Agilent 1260 Infinity system (pumps, degasser and UV-detector) connected to a motorized valve (BESTA Motorventil, Wilhelmsfeld, Germany) and a radiodetector (RamonaStar, Elysia-Raytest, Straubenhardt, Germany). A column switching method (*17*) was used to concentrate a lipophilic radiometabolite and the parent compound, while a more hydrophilic radiometabolite eluted from the column. Up to 5 mL plasma was directly injected into the HLB OASIS column (OASIS™ resin, Waters, Milford, MA, USA) with the mobile phase consisting of 1% acetonitrile and water. In an initial pilot study, a recovery rate of 99.6% was observed for the parent compound. After pump switching, HLB OASIS column was backflushed with a mobile phase consisting of 60% acetonitrile and 40% 50 mM ammonium acetate, pH 9. The second radiometabolite was separated from the parent compound using XSelect™ column (HSS T3, 3.5 µm, 100 × 4.6 mm, Waters, Milford, MA, USA) equipped with the corresponding pre-column. The areas under the curves were decay-corrected. The parent compound was identified by the retention time of the reference standard.

## Magnetic resonance imaging

Simultaneously with the PET acquisition, a structural T1-weighted image was acquired with a magnetization prepared rapid gradient echo sequence (MP-RAGE, TE/TR = 4.21/2200 ms, TI = 900 ms, flip angle = 9°, 160 sagittal slices, voxel size = 1x1x1.1 mm) for attenuation correction of the PET data, spatial normalization and to rule out structural abnormalities.

## PET processing

PET data were reconstructed with an ordinary Poisson ordered subset expectation-maximization algorithm (OP-OSEM, 3 iterations, 21 subsets) and binned into 12x5, 6x10, 3x20,

6x30, 9x60, 15x300 and 3x600 s frames. In addition to standard corrections, data were corrected for attenuation and scatter with a pseudoCT approach (*18*) based on the structural MRI of the first measurement.

Preprocessing was carried out with SPM12, as previously described (*19*). Briefly, PET data was corrected for head motion (quality setting = 1) and co-registered to the structural MRI. The structural MRI was spatially normalized to MNI space and the transformation matrix was applied to the co-registered PET images.

## Regions of interest

Time activity curves (TACs) were extracted for the following regions of interest (ROIs) from the Harvard-Oxford atlas and the probabilistic cerebellar atlas (https://fsl.fmrib.ox.ac.uk/fsl/fslwiki/Atlases): frontal, temporal, parietal, occipital, cingulate and somatosensory cortex as well as the subcortical regions thalamus, striatum, amygdala and hippocampus and the cerebellar grey matter, excluding the vermis. Additionally, the white matter structures centrum semiovale (extracted from the SPM12 tissue probability map), corpus callosum (from the Hammers N30R83 atlas (*20*)) and the cerebellar white matter (*21*) were investigated (Figure 2, top row). The left and corresponding right side of each ROI were averaged.

## Brain uptake

To investigate brain uptake and tracer distribution over time, standardized uptake values (SUV) were computed as activity concentration in tissue divided by administered dose per kg body weight. For further analyses and demonstration purposes, SUV TACs and SUV voxel-wise maps were averaged for the time points 5-30 min, 40-60 min, 70-90 min and 100-120 min.

In an exploratory approach, NMDAR binding (total volume of distribution, $V_T$) was quantified with the Logan plot using PMOD 4.2 (PMOD Technologies Ltd., Zurich, Switzerland;

www.pmod.com). For potential clinical applicability with high patient comfort, only the first 90 min of the data were used for the estimation of $V_T$. The start time of the fit of the Logan plot (t*) could not be determined automatically for the centrum semiovale because of high noise levels. Hence, the t* of the corpus callosum was used due to similar kinetics (Figure 3). A time-stability analysis was performed from 40–120 min for four regions with varying uptake (temporal and parietal cortex, striatum and hippocampus) to verify that measuring for 90 min is suitable.

A second exploratory analysis was conducted, quantifying $V_T$ with a constrained two-tissue compartment model with $K_1/k_2$ coupled (2TCM) for a measurement duration of 90 min. $K_1/k_2$ was estimated across all grey matter regions because of different kinetics in the white matter regions.

## Statistics

To assess the test-retest reliability, absolute percentage difference (APD), as well as the coefficient of variation (COV), were calculated between the two measurements for each ROI. Since there is no ground truth, the APD was determined as APD[%] = |m1-m2|/((m1+m2)/2)*100. COV[%] was calculated as (SD/mean)*100. The intraclass correlation coefficient (ICC) for absolute agreement was computed for each region of the averaged SUV time points. Finally, SUV averaged from 70-90 min was correlated with $V_T$ Logan plot estimated for 90 min across all regions of interest. Finally, $V_T$ Logan plot for 90 min was correlated with $V_T$ 2TCM.

# RESULTS

## Radiochemistry

After sterile filtration at the end of synthesis, 4.16 ± 1.31 GBq of *(R)*-$^{11}$C-Me-NB1 was obtained with a radiochemical purity of 97.5 ± 1.6%. Molar activity ranged from 35-1115 GBq/µmol (one value was excluded due to technical HPLC issues). All preparations were within the limits set by the European Pharmacopoeia.

## Blood data analysis

*(R)*-$^{11}$C-Me-NB1 was metabolized with 29.6 ± 5.5% of the parent fraction left after 20 min and 15.7 ± 3.3% after 40 min (Supplemental Figure 1A). Two radioactive metabolites were identified, which were more polar than the parent radioligand and showed baseline separation on the HPLC chromatograms (Supplemental Figure 1B and C).

## Brain uptake

The radioligand exhibited reversible pharmacokinetics (see $k_4$ obtained from 2TCM below) within the measurement time and an area-specific brain uptake pattern was observed (Figure 2, 3 and 4). At peak (~15-20 min post injection), SUV was highest in the striatum (4.5) and lowest in the white matter regions centrum semiovale and corpus callosum (both 1.8), followed by cerebellar white matter (2.6). Cortical regions showed similar kinetics, particularly after 60 min. In contrast, the kinetics of centrum semiovale and corpus callosum varied markedly from the other regions (Figure 3). Mean SUV TACs and standard deviations of representative regions are depicted in Supplemental Figure 2.

The time-stability analysis of the exploratory Logan plot revealed that measuring for 90 min is feasible with an underestimation of approximately 10% (Supplemental Figure 3, solid line). In addition, t* was evaluated as a function of measurement time (dashed line). Logan plots

of one representative subject are depicted in Supplemental Figure 4 to show linearity. The $V_T$ of the Logan plot varied between 12.8 in the corpus callosum and 19.0 ml/cm$^{-3}$ in the amygdala (Figure 4B). The average $V_T$ across all regions was comparable between the first and the second measurement (15.2 vs 15.9 ml/cm$^{-3}$).

For the 2TCM, the model did not converge for white matter regions (i.e. centrum semiovale, corpus callosum and cerebellar white matter). One subject did not show reasonable $V_T$ in one measurement and was therefore excluded from further analyses. The 2TCM confirmed the reversible binding with $k_4$ between 0.02 (somatosensory cortex) and 0.04 (cerebellar grey matter). $V_T$ 2TCM was slightly higher than with the Logan plot (Supplemental Figure 5).

A moderate correlation was achieved between Logan plot 90 min and SUV 70-90 min (Spearman's rho = 0.44). Spearman's rank correlation was used because of the presence of an outlier in $V_T$ in the test-retest analysis (Figure 5C). The correlation between $V_T$ Logan and 2TCM was good (r=0.76) with the caveat of one excluded subject and only grey matter regions (Supplemental Figure 5).

## Test-retest reliability

High test-retest reliability was obtained for SUV with slightly increasing values over time. Average APD across all ROIs was 6.9 vs 8.5% for SUV 5-30 min vs 100-120 min and COV was 4.9 vs 6.0% (Figure 5A). The ICC decreased from excellent (0.85 SUV 5-30 min) to moderate (0.58 SUV 100-120 min)

For $V_T$ Logan plot, the variability was slightly higher (mean APD 10.5%, mean COV 7.4%), which is caused by the same subject that did not show reasonable $V_T$ in the 2TCM (Figure 5B). In comparison, for $V_T$ 2TCM, mean APD was 8.2% and mean COV 5.8%, hence, slightly lower than with Logan plot (one subject excluded, only grey matter regions). Investigation

of the medians in Figure 5A and B exhibits similar APD between SUV and $V_T$ except for the centrum semiovale and the corpus callosum.

Complete lists of the SUV values for the various time points, $V_T$ for Logan plot and 2TCM for the test and retest measurement, alongside the values for APD and COV are shown in Supplemental Tables 1-4.

# DISCUSSION

In this study, the potential of *(R)*-$^{11}$C-Me-NB1, a selective and specific radioligand for imaging the GluN2B-subunits of the NMDA receptor in rodents, was examined for its performance characteristics in humans and utility in a clinical setting.

*(R)*-$^{11}$C-Me-NB1 has a number of advantages over previously published GluN2B PET radioligands (*10*). These include high specificity to the target receptor and topological distribution that matches the known expression pattern (*22*,*23*). Furthermore, the radioligand is easily and efficiently synthesized in good radiochemical yields using a one-step synthetic approach.

The results of the metabolite analysis showed the presence of two hydrophilic radiolabeled compounds, which were more polar than parent *(R)*-$^{11}$C-Me-NB1 and likely unable to cross the blood-brain barrier. This reasoning is based on previous studies in rodents that showed that more than 95% of radioactivity in rodent brain was intact *(R)*-$^{11}$C-Me-NB1 (*14*). In a recent study using mice liver microsomes, glucuronidation of the benzylic hydroxyl group and hydroxylation of the aromatic moiety in Me-NB1 were reported. Although we did not identify the radiometabolites, the HPLC profile suggests that the two hydrophilic radiometabolites may correspond to a hydroxylated species and the glucuronide of *(R)*-$^{11}$C-Me-NB1, respectively (*24*).

Brain uptake and distribution of *(R)*-$^{11}$C-Me-NB1 in humans were similar to rodent studies in most brain regions, including cortex, striatum and thalamus. However, while the cerebellum exhibited generally low radioligand uptake in rodents (*14*), cerebellar uptake in humans was region-dependent. Indeed, while the cerebellar white matter was among regions with limited tracer uptake, the cerebellar gray matter exhibited high *(R)*-$^{11}$C-Me-NB1 uptake in the present study. Whether the cerebellar uptake of *(R)*-$^{11}$C-Me-NB1 in humans reflects specific binding would need to be confirmed in blocking studies with GluN2B antagonists such as CP-101,606.

GluN2B subunit imaging in humans

An important feature of a useful radioligand is the pharmacokinetic profile for absolute quantification. In this regard, *(R)*-$^{11}$C-Me-NB1 exhibited reversible binding to the GluN2B-enriched NMDAR which was quantifiable with the Logan plot and 2TCM. The moderate correlation between $V_T$ and SUV 70-90 min might indicate a substitution of the absolute quantification but this requires further validation, including a comprehensive assessment of different modeling strategies.

Another benefit is the high test-retest reliability of around 8% (APD) for SUV and $V_T$ 2TCM and 11% for $V_T$ Logan plot, for a desirable measurement time of 90 min. The reliability is similar to other successfully translated radioligands (*25*), making it a promising tool for clinical applications.

We would like to acknowledge the small sample size of six subjects but suggest that this is acceptable for a first proof-of-concept study in humans. A limitation is that only young men were included. Hence, further work is required to assess potential sex differences and alterations with age.

The possibility to map GluN2B-enriched NMDAR in humans now enables receptor occupancy studies for drug development to treat neurodegenerative and other neuropsychiatric diseases. The notion is to modulate GluN2B-containing NMDAR with selective antagonists. However, substances such as EVT-101 or CERC-301 did show in vitro but not in vivo displacement of *(R)*-$^{11}$C-Me-NB1 in rodents (*14*) and limited efficacy in humans for CERC-301 (*8*). In contrast, CP-101,606 competed with *(R)*-$^{11}$C-Me-NB1 in rodents (*14*) and demonstrated similar antidepressant effects as ketamine in a clinical trial (*26*). However, the further development of the GluN2B antagonist was discontinued due to side effects (*27*). Hence, GluN2B-specific radioligands could aid the clinical investigations of the mechanism of action behind these drugs and the correlation between efficacy and receptor occupancy.

# CONCLUSION

For the first time, a GluN2B-subunit NMDAR-specific radioligand showing valuable characteristics in terms of pharmacokinetics and brain uptake was successfully translated into humans. A heterogeneous brain uptake with a robust test-retest variability (<10%) could be demonstrated. In an exploratory analysis, we could show that absolute quantification of the total volume of distribution with the Logan plot is feasible. The results suggest that *(R)*-$^{11}$C-Me-NB1 is a promising radioligand for visualizing the GluN2B-containing NMDA receptors in humans and potentially could be used in drug development programs to select appropriate doses of GluN2B-targeting drugs.

## DISCLOSURE / CONFLICT OF INTEREST

S. Ametamey and A. Haider are co-inventors of the filed patent number US2017/0224852A1. R. Lanzenberger received travel grants and/or conference speaker honoraria within the last three years from Bruker BioSpin MR and support from Siemens Healthcare regarding clinical research using PET/MR. He is a shareholder of the start-up company BM Health GmbH since 2019. Without relevance to this work, W. Wadsak received within the last 3 years research grants from ITM Medical Isotopes GmbH (Munich, Germany) and Scintomics (Fürstenfeldbruck, Germany). He is a part-time employee of CBmed GmbH (Graz, Austria) and a co-founder of MINUTE medical GmbH (Vienna, Austria). Without relevance to this work, M. Mitterhauser is scientific advisor for ROTOP Pharma GmbH. All other authors declared no potential conflicts of interest with respect to the research, authorship, and/or publication of this article.

## ACKNOWLEDGMENTS

This project was supported in part by the Swiss National Science Foundation grant numbers 310030E-160403/1 and 310030E-182872/1 to Prof. Simon M. Ametamey. Matej Murgaš is funded by the Austrian Science Fund FWF DOC 33-B27. Leo R. Silberbauer is a recipient of a DOC fellowship of the Austrian Academy of Sciences. The authors are particularly grateful to Dietmar Winkler, Pia Baldinger-Melich, Paul Michenthaler for clinical support. We thank Murray B. Reed, Vera Ritter, Daniel Pacher, Sebastian Klug, Marcel Koseler, Harald Ibeschitz, Natalie Schindler, Karsten Bamminger, Tim Wollenweber, Marius Ozenil for technical support. Furthermore, the authors thank Yves Auberson and Nicholas Seneca from Novartis also for their technical support.

# KEY POINTS

**Question:** Is *(R)*-$^{11}$C-Me-NB1 a suitable radioligand to map the GluN2B-containing N-methyl-D-aspartate receptor (NMDAR) in the human brain?

**Pertinent finding:** The radioligand demonstrated an area-specific brain uptake pattern with reversible pharmacokinetics and a high test-retest reliability.

**Implication for patient care:** The possibility to map the GluN2B-subunits of NMDAR provides new opportunities for the treatment of neuropsychiatric disorders such as Alzheimer's disease and major depression in terms of drug development.

# REFERENCES

1. Dingledine R, Borges K, Bowie D, Traynelis SF. The glutamate receptor ion channels. *Pharmacol Rev*. 1999;51:7-61.

2. Bliss TVP, Collingridge GL. A synaptic model of memory: long-term potentiation in the hippocampus. *Nature*. 1993;361:31-9.

3. Sattler R, Tymianski M. Molecular mechanisms of calcium-dependent excitotoxicity. *J Mol Med*. 2000;78:3-13.

4. Hardingham GE, Bading H. Synaptic versus extrasynaptic NMDA receptor signalling: implications for neurodegenerative disorders. *Nat Rev Neurosci*. 2010;11:682-96.

5. Ikonomidou C, Turski L. Why did NMDA receptor antagonists fail clinical trials for stroke and traumatic brain injury? *Lancet Neurol*. 2002;1:383-386.

6. Mony L, Kew JNC, Gunthorpe MJ, Paoletti P. Allosteric modulators of NR2B-containing NMDA receptors: molecular mechanisms and therapeutic potential. *Br J Pharmacol*. 2009;157:1301-1317.

7. Ahmed H, Haider A, Ametamey SM. N-Methyl-D-Aspartate (NMDA) receptor modulators: a patent review (2015-present). *Expert Opin Ther Pat*. 2020;30:743-767.

8. Ibrahim L, Diaz Granados N, Jolkovsky L, et al. A Randomized, placebo-controlled, crossover pilot trial of the oral selective NR2B antagonist MK-0657 in patients with treatment-resistant major depressive disorder. *J Clin Psychopharmacol*. 2012;32:551-7.

9. Gruber S, Ametamey SM. Imaging the glutamate receptor subtypes-Much achieved, and still much to do. *Drug Discov Today Technol*. 2017;25:27-36.

10. Fuchigami T, Nakayama M, Yoshida S. Development of PET and SPECT probes for glutamate receptors. *Sci World J*. 2015;2015:1-19.

11. Fu H, Tang W, Chen Z, et al. Synthesis and preliminary evaluations of a triazole-cored antagonist as a PET imaging probe ([18F]N2B-0518) for GluN2B subunit in the brain. *ACS Chem Neurosci*. 2019;10:2263-2275.

12. Ahmed H, Haider A, Varisco J, et al. Structure–affinity relationships of 2,3,4,5-Tetrahydro-1 H -3-benzazepine and 6,7,8,9-Tetrahydro-5 H -benzo[7]annulen-7-amine analogues and the discovery of a radiofluorinated 2,3,4,5-Tetrahydro-1 H -3-benzazepine congener for imaging GluN2B subunit-containing N-Methyl-d-Aspartate receptors. *J Med Chem*. 2019;62:9450-9470.

13. Ahmed H, Wallimann R, Haider A, et al. Preclinical development of 18F-OF-NB1 for imaging GluN2B-containing N-Methyl-d-Aspartate receptors and its utility as a biomarker for amyotrophic lateral sclerosis. *J Nucl Med*. 2021;62:259-265.

14. Haider A, Herde AM, Krämer SD, et al. Preclinical evaluation of benzazepine-based PET radioligands (R)- and (S)-11C-Me-NB1 reveals distinct enantiomeric binding patterns and a tightrope walk between GluN2B- and σ1-receptor-targeted PET imaging. *J Nucl Med*. 2019;60:1167-1173.

15. Krämer SD, Betzel T, Mu L, et al. Evaluation of 11 C-Me-NB1 as a potential PET radioligand for measuring GluN2B-containing NMDA receptors, drug occupancy, and receptor cross talk. *J Nucl Med*. 2018;59:698-703.

16. Radiopharmaceutical Preparations. (Radiopharmaceutica, 8.0/1483). European Pharmacopoeia (Europäisches Arzneibuch). 8th ed. Vienna: Official Austrian Version, Verlag Oesterreich GmbH; 2008; 1167–73(8. Ausgabe Grundwerk).

17. Vasdev N, Collier T. Design and prototype of an automated column-switching HPLC system for radiometabolite analysis. *Pharmaceuticals*. 2016;9:51.

18. Burgos N, Cardoso MJ, Thielemans K, et al. Attenuation correction synthesis for hybrid PET-MR scanners: Application to brain studies. *IEEE Trans Med Imaging*. 2014;33:2332-2341.

19. Rischka L, Gryglewski G, Pfaff S, et al. Reduced task durations in functional PET imaging with [18F]FDG approaching that of functional MRI. *Neuroimage*. 2018;181:323-330.

20. Gousias IS, Rueckert D, Heckemann RA, et al. Automatic segmentation of brain MRIs of 2-year-olds into 83 regions of interest. *Neuroimage*. 2008;40:672-684.

21. van Baarsen KM, Kleinnijenhuis M, Jbabdi S, Sotiropoulos SN, Grotenhuis JA, van Cappellen van Walsum AM. A probabilistic atlas of the cerebellar white matter. *Neuroimage*. 2016;124:724-732.

22. Rigby M, Le Bourdellès B, Heavens RP, et al. The messenger RNAs for the N-methyl-D-aspartate receptor subunits show region-specific expression of different subunit composition in the human brain. *Neuroscience*. 1996;73:429-447.

23. Enoch MA, Rosser AA, Zhou Z, Mash DC, Yuan Q, Goldman D. Expression of glutamatergic genes in healthy humans across 16 brain regions; Altered expression in the hippocampus after chronic exposure to alcohol or cocaine. *Genes, Brain Behav*. 2014;13:758-768.

24. Börgel F, Galla F, Lehmkuhl K, Schepmann D, Ametamey SM, Wünsch B. Pharmacokinetic properties of enantiomerically pure GluN2B selective NMDA receptor antagonists with 3-benzazepine scaffold. *J Pharm Biomed Anal*. 2019;172:214-222.

25. Nord M, Finnema SJ, Schain M, Halldin C, Farde L. Test-retest reliability of [11C]AZ10419369 binding to 5-HT(1B) receptors in human brain. *Eur J Nucl Med Mol Imaging*. 2014;41:301-7.

26. Preskorn SH, Baker B, Kolluri S, Menniti FS, Krams M, Landen JW. An innovative design to establish proof of concept of the antidepressant effects of the NR2B subunit selective N-Methyl-D-Aspartate antagonist, CP-101,606, in patients with treatment-refractory major depressive disorder. *J Clin Psychopharmacol*. 2008;28:631-637.

27. Machado-Vieira R, Henter ID, Zarate CA. New targets for rapid antidepressant action. *Prog Neurobiol*. 2017;152:21-37.

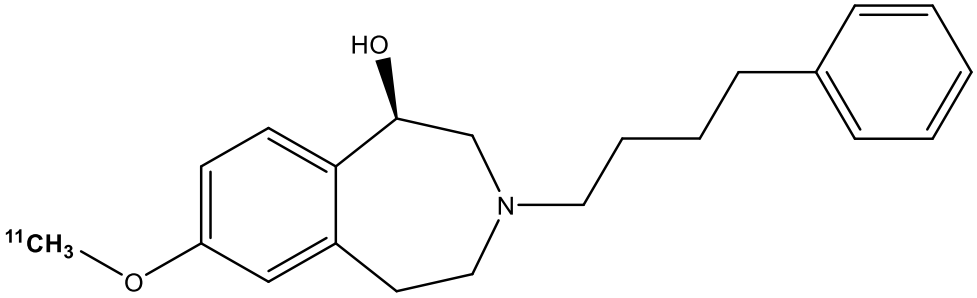


**Figure 1:** *Chemical structure of (R)-*$^{11}$C*-Me-NB1*.

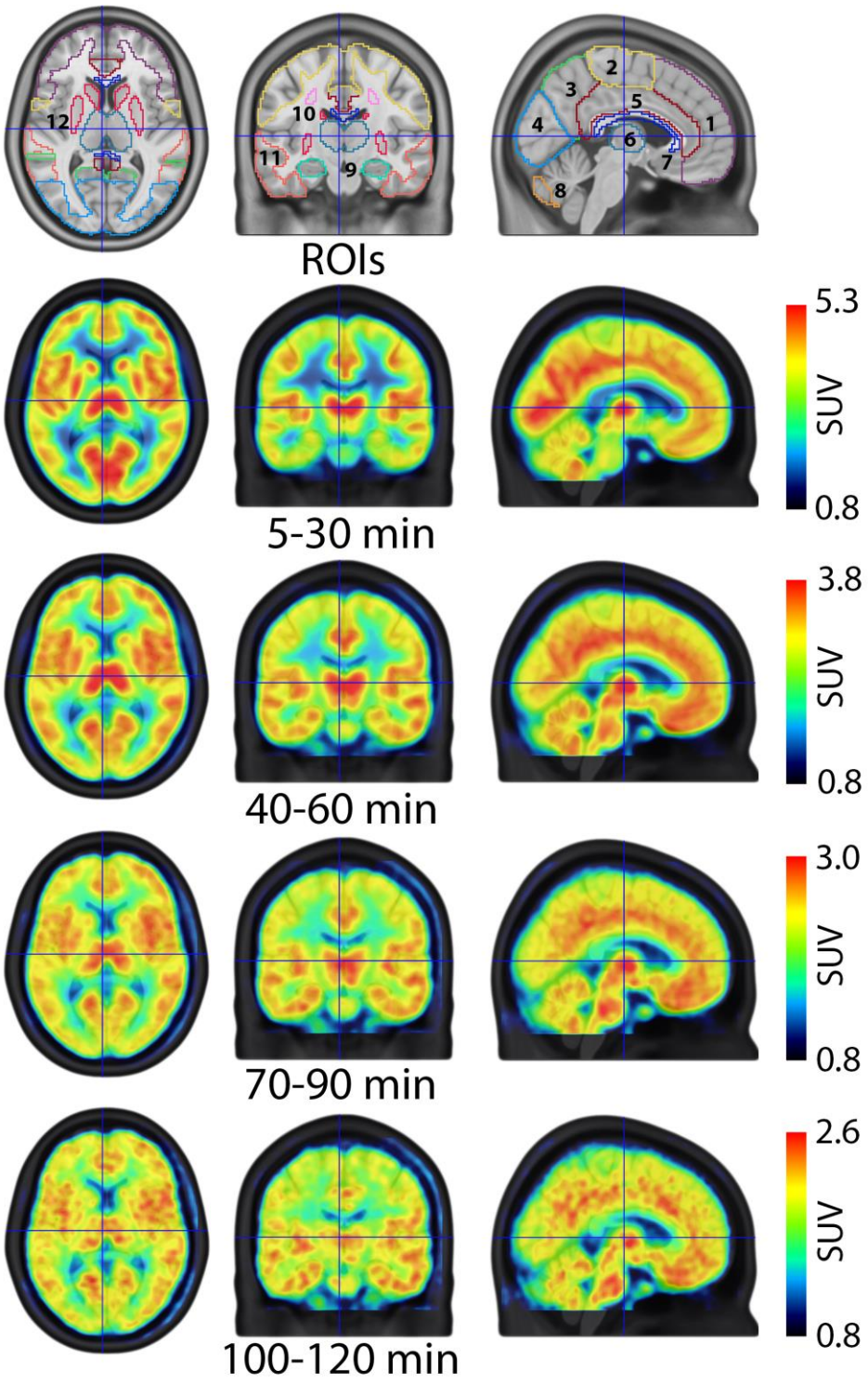


**Figure 2:** *Regions of interest (ROIs) and mean standardized uptake value (SUV) maps*. The first row depicts the investigated ROIs covering cortical, subcortical and white matter structures: 1: frontal cortex, 2: somatosensory cortex, 3: parietal cortex, 4: occipital cortex, 5: cingulate cortex,

6: thalamus, 7: corpus callosum, 8: cerebellar gray matter, 9: hippocampus, 10: centrum semiovale, 11: temporal cortex, 12: striatum. Amygdala and cerebellar white matter are not visible in the presented slices (MNI space, x =-4, y = 16, z= 7 mm). The remaining rows depict the radioligand distribution in terms of SUV for various time points (averaged across subjects).

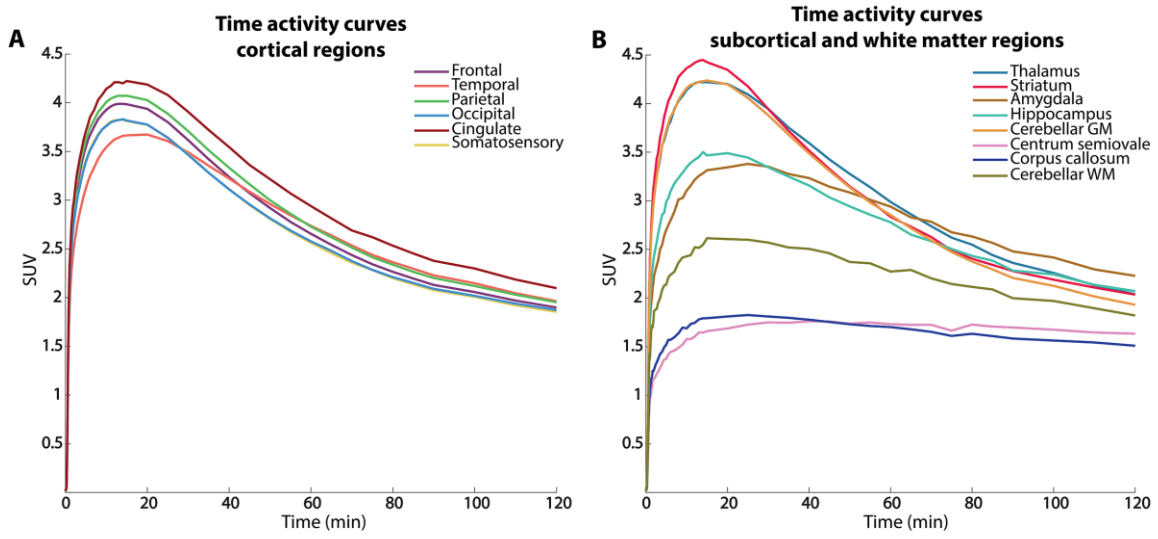


**Figure 3:** *Kinetics of (R)-*$^{11}$C*-Me-NB1.* Reversible kinetics were obtained within the measurement time. A) Time activity curves demonstrate homogeneous kinetics in cortical regions. B) Subcortical regions showed variable kinetics with highest uptake observed in the striatum. Lowest SUV and markedly different kinetics were observed in the centrum semiovale and corpus callosum.

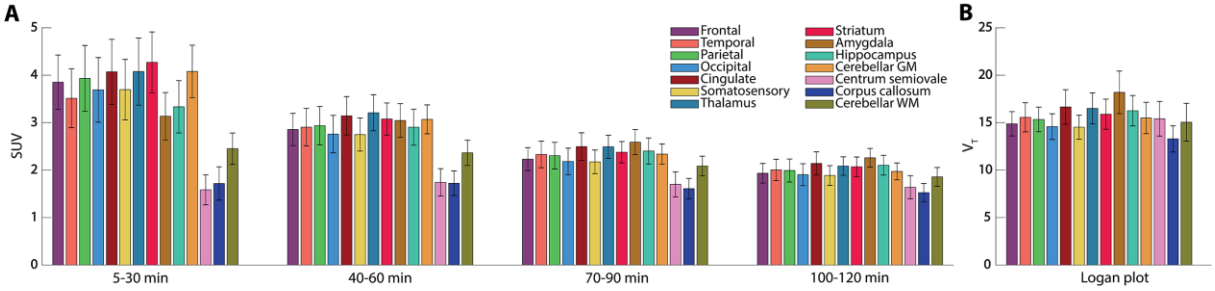


**Figure 4:** *SUV and $V_T$ using Logan plot.* A) SUV of each ROI for several time points. B) Exploratory $V_T$ computed with the Logan plot.

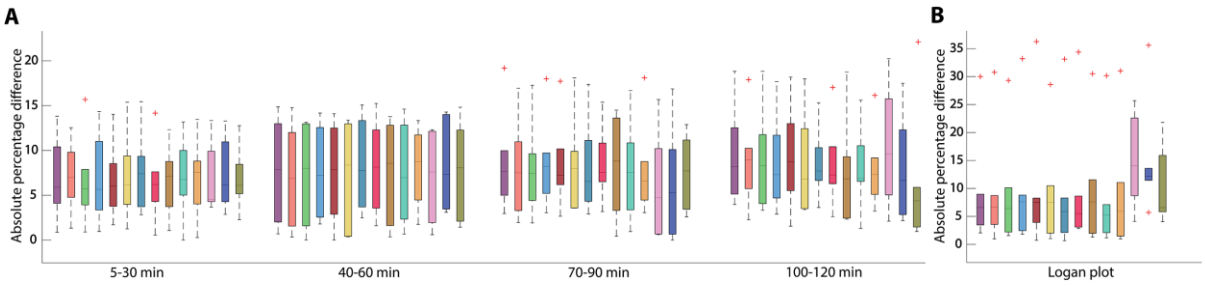


***Figure 5:*** *Absolute percentage difference (APD) of SUV and Logan plot.* A) The APD of the SUV is comparable over time in most regions with slightly larger interquartile ranges for 40-60 mins. B) The APD of the Logan plot visualizes similar median differences as for SUV but with one outlier. The colors match the regions in Figure 4.

Graphical Abstract

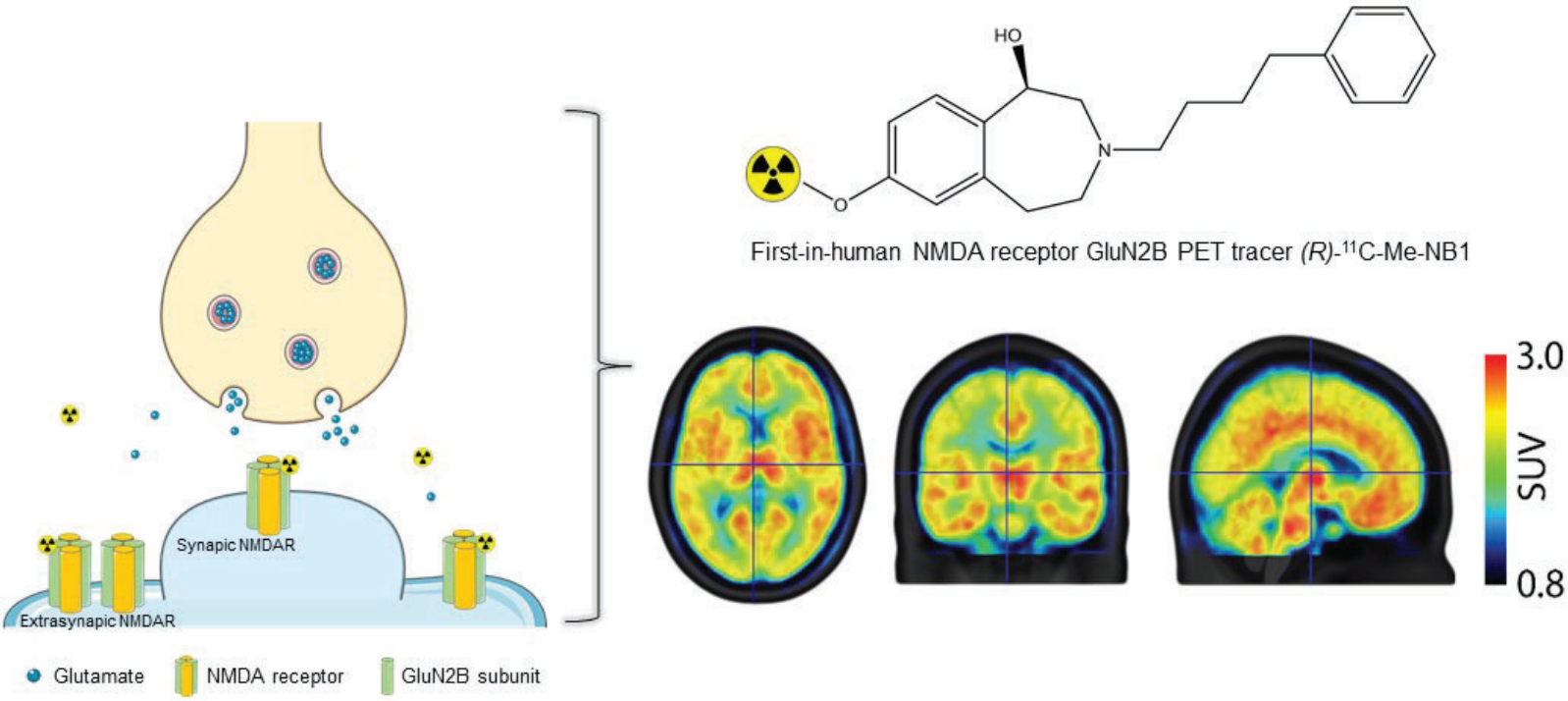

# Supplementary material

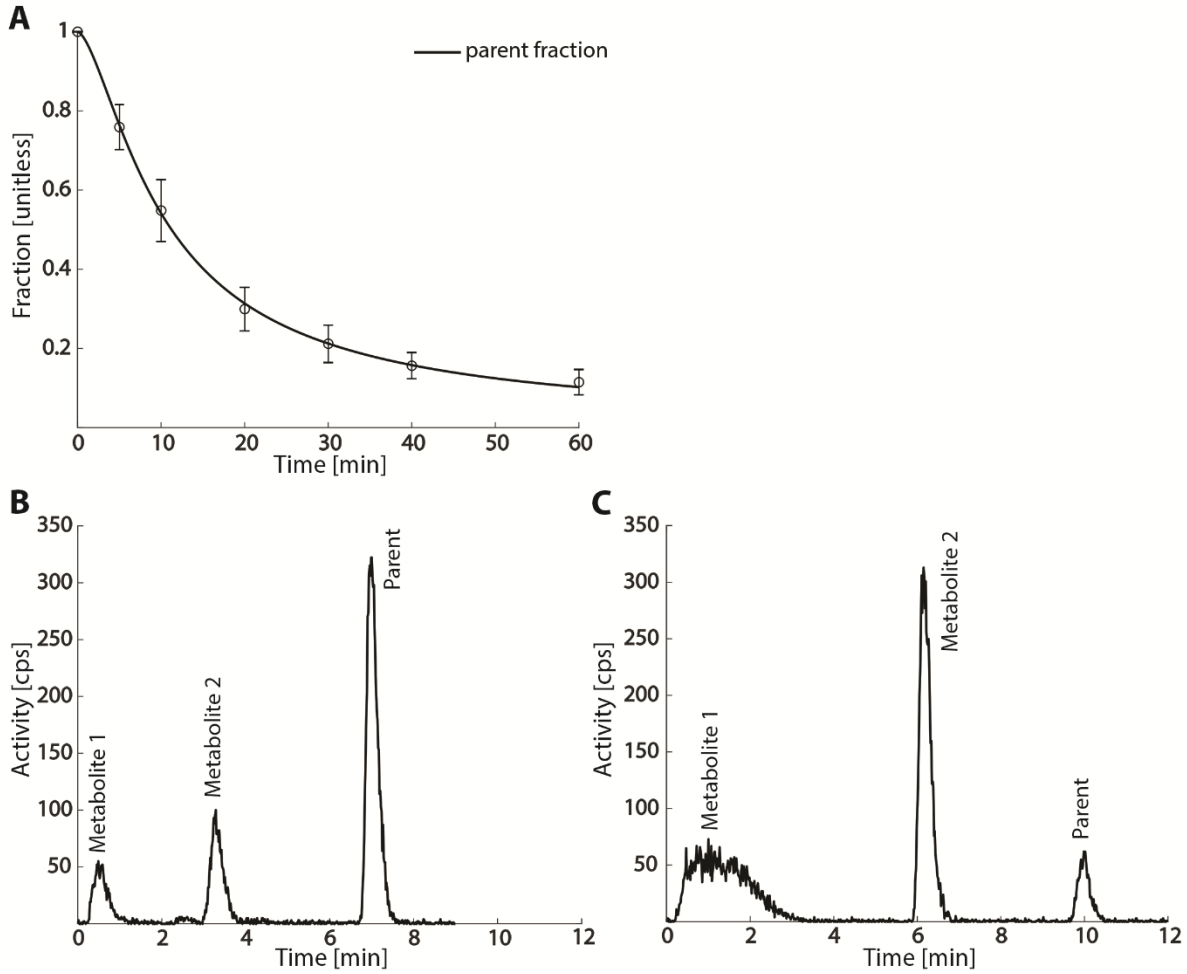


***Supplemental Figure 1:*** *Metabolite data. A*) *(R)*-[$^{11}$C]-Me-NB1 was quickly metabolized with ~30% of the parent compound left after 20 minutes. B) and C) The radioactive metabolites shown for 5 and 40 min were well separated from the parent compound yielding an accurate parent fraction. Injection volume of plasma is increased over time up to 5 mL. Therefore, retention times (Rt) using this column switching method are delayed with later blood sampling time points. Corrected Rts based on the column switching time are 1.3 and 5.1 min for the second metabolite and the parent compound, respectively.

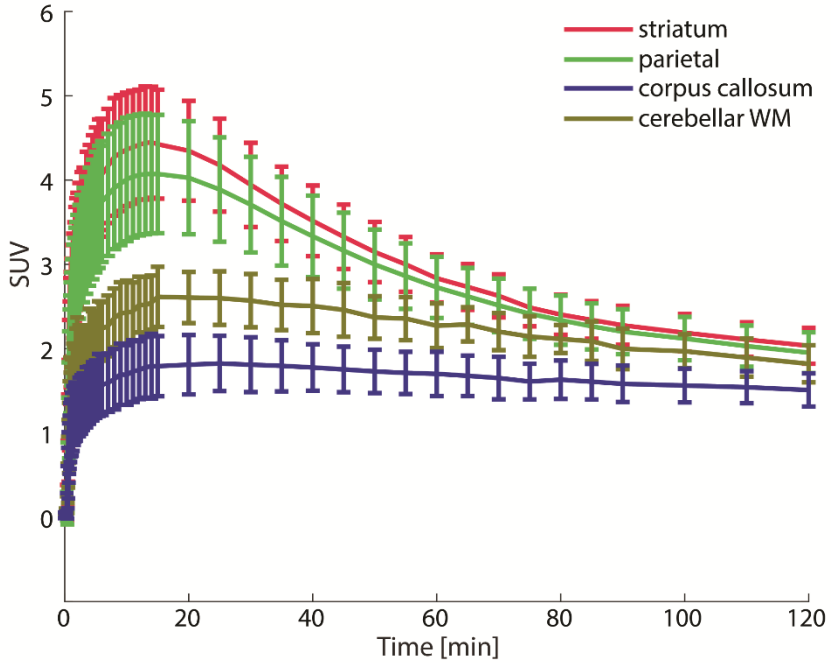


**Supplemental Figure 2**: *Mean SUV TACs with standard deviation of representative regions*.

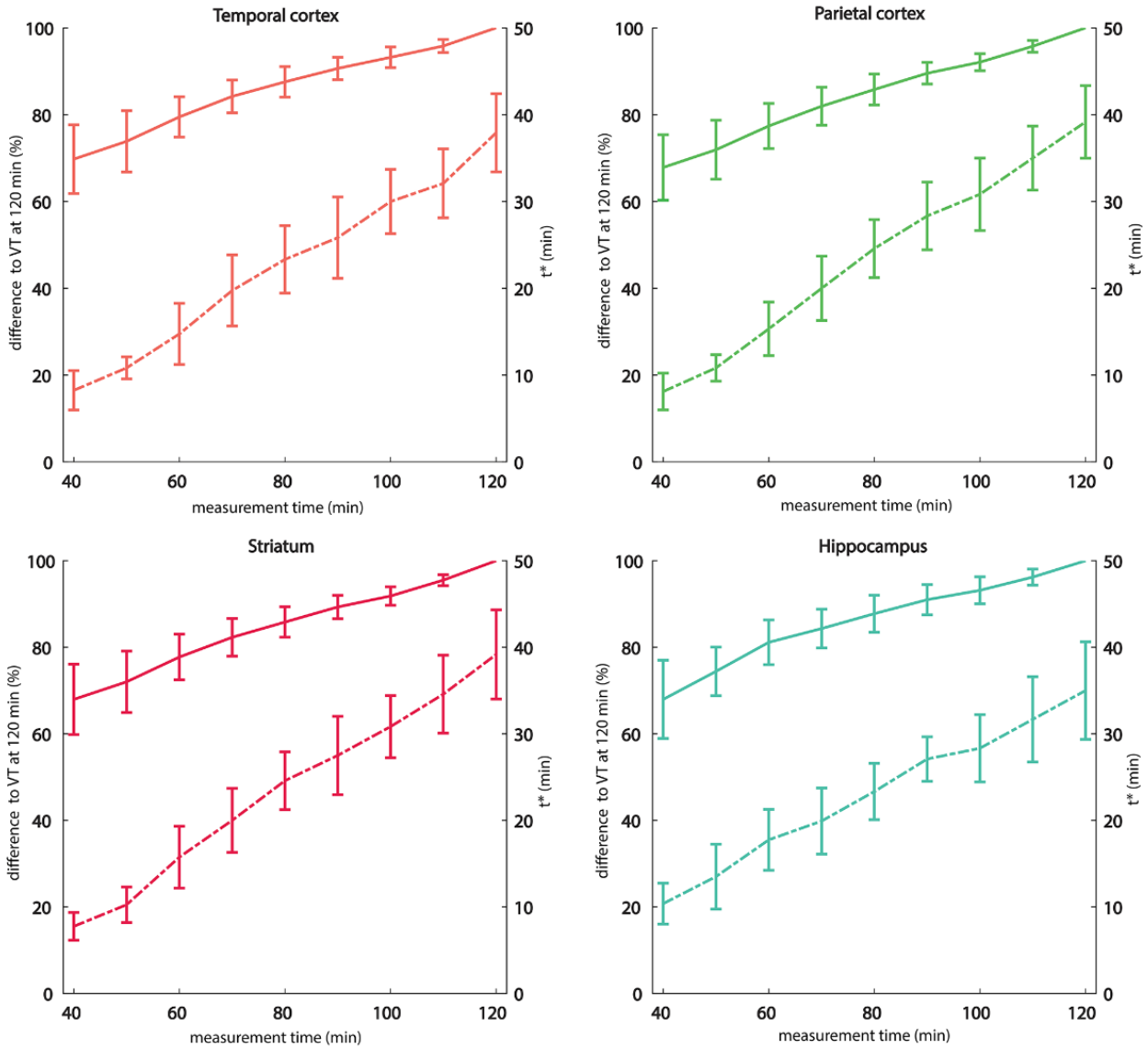


**Supplemental Figure 3:** *Time-stability analysis of Logan plot $V_T$ and t*.* The time-stability analysis exhibits an underestimation of $V_T$ of around 10% for Logan plot 90 min in comparison to 120 min (solid line). The t* for 90 min was around 25 min (dashed line).

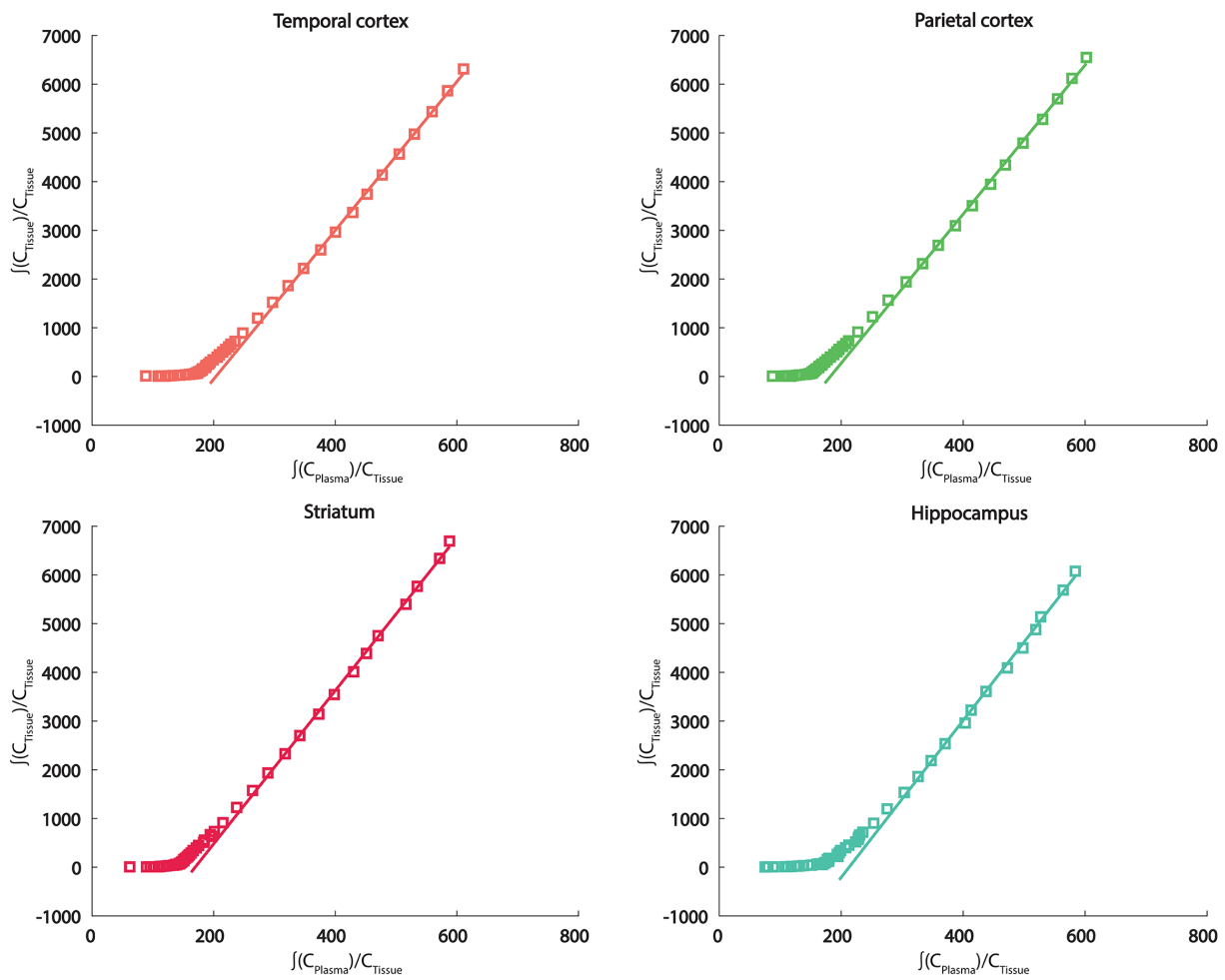


**Supplemental Figure 4:** *Logan plots of four regions with varying uptake*. Logan plots of one representative subject are shown, demonstrating that linearity is reached and thus, Logan plot for a 90 min measurement is a feasible method to quantify $V_T$.

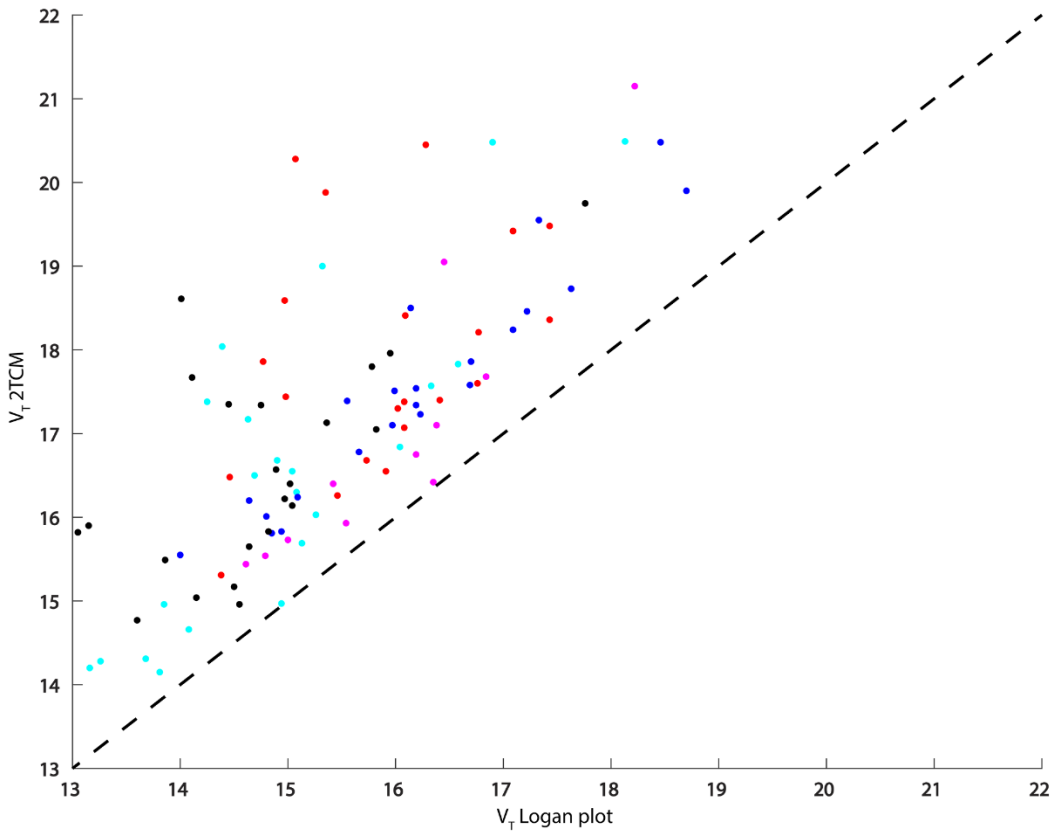


**Supplemental Figure 5:** *Comparison of $V_T$ Logan plot and 2TCM.* For 2TCM, $V_T$ was slightly higher than with Logan plot. The dashed line represents the line of identity. Subjects are identified by the same color, including both measurements and all grey matter regions. One subject had to be excluded due to unreasonable results in 2TCM.

| | | frontal | temporal | parietal | occipital | cingulate | somatosensory | thalamus | striatum |
|---|---|---|---|---|---|---|---|---|---|
| SUV | M1 | 3.8±0.5 | 3.5±0.5 | 3.9±0.6 | 3.6±0.6 | 4.0±0.6 | 3.6±0.5 | 4.0±0.6 | 4.2±0.6 |
| 5-30 min | M2 | 3.9±0.7 | 3.6±0.7 | 4.0±0.8 | 3.8±0.8 | 4.1±0.8 | 3.7±0.8 | 4.1±0.9 | 4.3±0.8 |
| SUV | M1 | 2.8±0.2 | 2.9±0.3 | 2.9±0.3 | 2.7±0.3 | 3.1±0.3 | 2.7±0.2 | 3.2±0.2 | 3.0±0.2 |
| 40-60 min | M2 | 2.9±0.4 | 3.0±0.5 | 3.0±0.5 | 2.8±0.5 | 3.2±0.5 | 2.8±0.5 | 3.3±0.5 | 3.1±0.5 |
| SUV | M1 | 2.2±0.2 | 2.3±0.2 | 2.3±0.2 | 2.2±0.2 | 2.5±0.2 | 2.2±0.2 | 2.5±0.2 | 2.3±0.2 |
| 70-90 min | M2 | 2.3±0.3 | 2.4±0.4 | 2.3±0.3 | 2.2±0.3 | 2.5±0.4 | 2.2±0.3 | 2.5±0.3 | 2.4±0.3 |
| SUV | M1 | 1.9±0.2 | 2.0±0.2 | 2.0±0.2 | 1.9±0.2 | 2.1±0.2 | 1.9±0.2 | 2.1±0.2 | 2.1±0.2 |
| 100-120 min | M2 | 2.0±0.2 | 2.0±0.3 | 2.0±0.3 | 1.9±0.3 | 2.2±0.3 | 1.9±0.2 | 2.1±0.2 | 2.1±0.2 |

| | | amygdala | hippocampus | cerebellar GM | c. semiovale | corpus callosum | cerebellar WM | mean |
|---|---|---|---|---|---|---|---|---|
| SUV | M1 | 3.1±0.4 | 3.3±0.5 | 4.0±0.5 | 1.6±0.3 | 1.7±0.3 | 2.4±0.3 | 3.3±0.9 |
| 5-30 min | M2 | 3.2±0.6 | 3.4±0.7 | 4.1±0.7 | 1.6±0.4 | 1.7±0.4 | 2.5±0.4 | 3.4±0.9 |
| SUV | M1 | 3.0±0.2 | 2.9±0.3 | 3.1±0.2 | 1.7±0.2 | 1.7±0.2 | 2.3±0.2 | 2.7±0.5 |
| 40-60 min | M2 | 3.1±0.5 | 3.0±0.5 | 3.1±0.4 | 1.8±0.4 | 1.7±0.3 | 2.4±0.3 | 2.8±0.5 |
| SUV | M1 | 2.5±0.2 | 2.4±0.2 | 2.3±0.2 | 1.7±0.2 | 1.6±0.2 | 2.1±0.2 | 2.2±0.3 |
| 70-90 min | M2 | 2.6±0.4 | 2.4±0.4 | 2.3±0.3 | 1.7±0.3 | 1.6±0.3 | 2.1±0.3 | 2.3±0.3 |
| SUV | M1 | 2.3±0.2 | 2.1±0.2 | 2±0.2 | 1.6±0.2 | 1.5±0.2 | 1.9±0.2 | 1.9±0.2 |
| 100-120 min | M2 | 2.3±0.2 | 2.1±0.3 | 2±0.2 | 1.7±0.3 | 1.5±0.2 | 1.8±0.2 | 2.0±0.2 |

***Supplemental Table 1:*** *Mean standardized uptake values (SUV) for various time points for measurement 1 and 2 for all investigated regions.*

| | | frontal | temporal | parietal | occipital | cingulate | somatosensory | thalamus | striatum |
|---|---|---|---|---|---|---|---|---|---|
| Logan | M1 | 14.7±1.1 | 15.3±1.1 | 15.1±1.2 | 14.3±1.3 | 16.3±1.2 | 14.3± 1.0 | 16.2±0.9 | 15.6±0.9 |
| 90 min | M2 | 15.1±1.5 | 15.8±1.9 | 15.6±1.5 | 14.9±1.5 | 17.0±2.4 | 14.7±1.6 | 16.8±2.2 | 16.2±2.1 |
| 2TCM* | M1 | 16.7±1.4 | 16.7±1.2 | 16.7±0.9 | 17.4±1.7 | 17.6±1.1 | 17.4±1.8 | 17.7±0.9 | 16.6±1.0 |
| 90 min | M2 | 16.0±1.1 | 16.2±0.7 | 16.2±1.0 | 16.2±1.4 | 17.1±0.9 | 16.4±1.8 | 17.0±0.6 | 16.0±0.6 |

| | | amygdala | hippocampus | cerebellar GM | c. semiovale | corpus callosum | cerebellar WM | mean |
|---|---|---|---|---|---|---|---|---|
| Logan | M1 | 17.4±1.0 | 15.9±0.9 | 15.3±1 | 15.5±2.1 | 12.8±1.3 | 14.5±1.3 | 15.2±1.1 |
| 90 min | M2 | 19.0± 2.9 | 16.6±2.1 | 15.6±2.2 | 15.4±1.8 | 13.7±1.4 | 15.6±2.6 | 15.9±1.3 |
| 2TCM* | M1 | 19.2±1.4 | 18.8±1.4 | 16.4±1.0 | - | - | - | 17.4±1.3 |
| 90 min | M2 | 20.2±0.7 | 18.2±0.7 | 15.5±0.9 | - | - | - | 16.8±1.0 |

**Supplemental Table 2**: *Mean total volume of distribution ($V_T$) computed with Logan and 2TCM for all investigated regions*. Of note, 2TCM only converged for grey matter regions. One subject had to be excluded from the 2TCM analyses due to unreasonable results (indicated by the *).

| | | frontal | temporal | parietal | occipital | cingulate | somatosensory | thalamus | striatum |
|---|---|---|---|---|---|---|---|---|---|
| SUV | APD | 6.8±3.3 | 7.1±2.9 | 6.6±3.6 | 6.8±3.6 | 6.7±3.0 | 7.1±3.6 | 7.7±3.2 | 6.5±3.2 |
| 5-30 min | COV | 4.8±3.3 | 5.0±2.9 | 4.7±3.6 | 4.8±3.6 | 4.7±3.0 | 5.0±3.6 | 5.4±3.2 | 4.6±3.2 |
| | ICC | 0.83 | 0.88 | 0.86 | 0.87 | 0.87 | 0.85 | 0.84 | 0.84 |
| SUV | APD | 7.7±4.3 | 7.1±4.4 | 7.3±4.4 | 7.6±4.1 | 7.5±4.2 | 7.3±4.5 | 8.3±3.9 | 8.2± 4.0 |
| 40-60 min | COV | 5.4±4.3 | 5.0±4.4 | 5.2±4.4 | 5.4±4.1 | 5.3±4.2 | 5.2±4.5 | 5.9±3.9 | 5.8± 4.0 |
| | ICC | 0.65 | 0.75 | 0.75 | 0.77 | 0.72 | 0.70 | 0.62 | 0.59 |
| SUV | APD | 8.7±4.0 | 8.0±3.9 | 8.0±3.8 | 8.7±3.7 | 8.5±3.6 | 8.5±3.8 | 8.1±3.8 | 8.5± 3.0 |
| 70-90 min | COV | 6.2± 4.0 | 5.7±3.9 | 5.7±3.8 | 6.2±3.7 | 6.0±3.6 | 6.0±3.8 | 5.8±3.8 | 6.0±3.0 |
| | ICC | 0.55 | 0.69 | 0.71 | 0.71 | 0.66 | 0.63 | 0.52 | 0.52 |
| SUV | APD | 9.5± 4.0 | 9.0±3.7 | 9.1±4.0 | 8.6±3.8 | 9.3±4.2 | 8.5±4.1 | 8.6±2.8 | 8.5±3.5 |
| 100-120 min | COV | 6.7± 4.0 | 6.4±3.7 | 6.4± 4.0 | 6.1±3.8 | 6.6±4.2 | 6.0±4.1 | 6.0±2.8 | 6.0±3.5 |
| | ICC | 0.50 | 0.61 | 0.65 | 0.69 | 0.59 | 0.60 | 0.51 | 0.55 |

| | | amygdala | hippocampus | cerebellar GM | c. semiovale | corpus callosum | cerebellar WM | mean |
|---|---|---|---|---|---|---|---|---|
| SUV | APD | 6.7±2.8 | 7.0±3.2 | 7.0±3.2 | 6.7±2.8 | 7.3±2.8 | 6.8±2.5 | 6.9±0.3 |
| 5-30 min | COV | 4.7±2.8 | 4.9±3.2 | 4.9±3.2 | 4.7±2.8 | 5.2±2.8 | 4.8±2.5 | 4.9±0.2 |
| | ICC | 0.87 | 0.86 | 0.80 | 0.90 | 0.90 | 0.82 | 0.85 |
| SUV | APD | 7.6±4.4 | 7.4±4.4 | 8.1±3.3 | 7.0±3.8 | 8.2±3.8 | 7.8±3.9 | 7.7±0.4 |
| 40-60 min | COV | 5.4±4.4 | 5.2±4.4 | 5.7±3.3 | 5.0±3.8 | 5.8±3.8 | 5.5±3.9 | 5.4±0.3 |
| | ICC | 0.64 | 0.72 | 0.53 | 0.85 | 0.78 | 0.63 | 0.69 |
| SUV | APD | 8.2±4.1 | 7.8±4.2 | 7.9±3.8 | 6.1±4.4 | 6.4±4.8 | 7.6±3.1 | 7.9±0.8 |
| 70-90 min | COV | 5.8±4.1 | 5.5±4.2 | 5.6±3.8 | 4.3±4.4 | 4.5±4.8 | 5.4±3.1 | 5.6±0.6 |
| | ICC | 0.53 | 0.65 | 0.44 | 0.86 | 0.75 | 0.60 | 0.63 |
| SUV | APD | 7.7±4.3 | 8.0±3.4 | 8.0±3.2 | 10.4±4.7 | 8.0±4.4 | 6.5±5.6 | 8.5±0.9 |
| 100-120 min | COV | 5.5±4.3 | 5.6±3.4 | 5.7±3.2 | 7.4±4.7 | 5.7±4.4 | 4.6±5.6 | 6.0±0.6 |
| | ICC | 0.41 | 0.61 | 0.49 | 0.65 | 0.70 | 0.61 | 0.58 |

***Supplemental Table 3****: Absolute percentage difference, coefficient of variation and intraclass correlation coefficient for each region for SUV values.* See Supplemental Table 1 for detailed legend

| | | frontal | temporal | parietal | occipital | cingulate | somatosensory | thalamus | striatum |
|---|---|---|---|---|---|---|---|---|---|
| Logan | APD | 9.6±10.3 | 9.6±10.8 | 9.3±10.3 | 10.2±11.6 | 10.7±12.8 | 9.5± 10.0 | 9.3±12.0 | 10.0±12.2 |
| 90 min | COV | 6.8±7.3 | 6.8±7.6 | 6.6±7.3 | 7.2±8.2 | 7.6±9.1 | 6.7±7.1 | 6.6±8.5 | 7.1±8.6 |
| 2TCM | APD | 10.9±5.1 | 6.9±4.0 | 7.8±4.6 | 11.4±7.7 | 7.7±4.5 | 12.6±6.5 | 6.3±3.6 | 6.9±4.4 |
| 90 min | COV | 7.7±3.6 | 4.9±2.8 | 5.5±3.2 | 8.1±5.4 | 5.5±3.2 | 8.9±4.6 | 4.5±2.5 | 4.9±3.1 |

| | | amygdala | hippocampus | cerebellar GM | c. semiovale | corpus callosum | cerebellar WM | mean |
|---|---|---|---|---|---|---|---|---|
| Logan | APD | 10.1±10.7 | 8.5±10.9 | 9.4±11.4 | 14.9± 8.2 | 15.1±10.4 | 10.1±7.1 | 10.5±2.0 |
| 90 min | COV | 7.1±7.6 | 6.0±7.7 | 6.6±8.0 | 10.5±5.8 | 10.7±7.4 | 7.2±5.0 | 7.4±1.4 |
| 2TCM* | APD | 6.0±6.8 | 7.2±3.2 | 6.8±5.1 | - | - | - | 8.2±5.0 |
| 90 min | COV | 4.2±4.8 | 5.1±2.2 | 4.8±3.6 | - | - | - | 5.8±3.6 |

**Supplemental Table 4:** *Absolute percentage difference and coefficient of variation for each region for $V_T$ values obtained from the Logan plot and 2TCM*. See Supplemental Table 3 for detailed legend.